Chemical Geology 667 (2024) 122318

Contents lists available at ScienceDirect

Chemical Geology

journal homepage: www.elsevier.com/locate/chemgeo

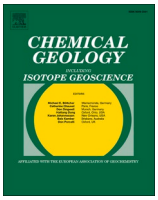

Nucleation-assisted microthermometry: A novel application to fluid inclusions in halite

William D. Arnuk [a,*], Emmanuel Guillerm [a,b], Tim K. Lowenstein [a], Yves Krüger [c], Kristian J. Olson [a], Nadav G. Lensky [d,e], Achim Brauer [b,f]

[a] Department of Earth Sciences, Binghamton University, 400 Vestal Pkwy E, Binghamton, NY 13902, USA
[b] GFZ German Research Centre for Geosciences, Section Climate Dynamics and Landscape Evolution, Telegrafenberg, 14473 Potsdam, Germany
[c] Department of Earth Science, University of Bergen, Bergen, Norway
[d] The Fredy and Nadine Herrmann Institute of Earth Sciences, Edmond J. Safra Campus, The Hebrew University of Jerusalem, Givat Ram, Jerusalem 91904, Israel
[e] Geological Survey of Israel, 32 Yesha'ayahu Leibowitz, Jerusalem 9692100, Israel
[f] Institute of Geosciences, University of Potsdam, 14476 Potsdam, Germany

ARTICLE INFO

Editor: Oleg Pokrovsky

Keywords:
Geochemistry
Aqueous geochemistry
Paleothermometry
Paleolimnology
Lakes
Evaporites
Halite
Fluid inclusions
Microthermometry
Salt
Dead Sea
Death Valley
Chemical sediments
Sedimentology
Paleoclimate
Paleoclimate proxies

ABSTRACT

Halite deposits have long been utilized for interrogating past climate conditions. Microthermometry on halite fluid inclusions has been used to determine ancient water temperatures. One notable obstacle in performing microthermometric measurements, however, is the lack of a vapor bubble in the single-phase liquid inclusions at room temperature. (Pseudo-) isochoric cooling of the inclusions to high negative pressures, far below the homogenization temperature, has commonly been needed to provoke spontaneous vapor bubble nucleation in the liquid. High internal tensile stress in soft host minerals like halite, however, may induce plastic deformation of the inclusion walls, resulting in a wide scatter of measured homogenization temperatures. Nucleation-assisted (NA) microthermometry, in contrast, employs single ultra-short laser pulses provided by a femtosecond laser to stimulate vapor bubble nucleation in metastable liquid inclusions slightly below the expected homogenization temperature. This technique allows for repeated vapor bubble nucleation in selected fluid inclusions without affecting the volumetric properties of the inclusions, and yields highly precise and accurate homogenization temperatures.

In this study, we apply, for the first time, NA microthermometry to fluid inclusions in halite and we evaluate the precision and accuracy of this thermometer utilizing (i) synthetic halite crystals precipitated under controlled laboratory conditions, (ii) modern natural halite that precipitated in the 1980s in the Dead Sea, and (iii) Late Pleistocene halite samples from a sediment core from Death Valley, CA. Our results demonstrate an unprecedented accuracy and precision of the method that provides a new opportunity to reconstruct reliable quantitative temperature records from evaporite archives.

1. Introduction

Our understanding of paleoclimatic conditions on Earth relies on the diversity of archives that record information at various spatial and temporal scales as well as an ensemble of proxy methods that allow us to interrogate climatic conditions from those archives. Halite-bearing evaporites constitute a valuable climate archive that is global in extent, and undeformed deposits occur as far back as the Neoproterozoic (Warren, 2010; Bąbel and Schreiber, 2014; Spear et al., 2014). These deposits preserve a wealth of information about water budget and/or lake levels (Lowenstein and Hardie, 1985; Li et al., 1996; Schreiber and Tabakh, 2000; Rigaudier et al., 2011; Kiro et al., 2017; Sirota et al., 2018; Guillerm et al., 2023), lake and seawater chemistry (Lowenstein et al., 2001, 2016; Zimmermann, 2001; Rigaudier et al., 2012; Brennan et al., 2013; Weldeghebriel et al., 2022; Weldeghebriel and Lowenstein, 2023), and, with sodium carbonate minerals, atmospheric pCO_2 (Lowenstein and Demicco, 2006; Jagniecki et al., 2015; Olson and Lowenstein, 2021). Furthermore, fluid inclusions in halite crystals also provide information on brine temperatures at the time of precipitation.

Fluid inclusion microthermometry is a purely physical thermometer that uses the density of the aqueous solution enclosed in microscopic crystal cavities to assess mineral formation temperatures by means of

* Corresponding author.
E-mail address: warnuk1@binghamton.edu (W.D. Arnuk).

https://doi.org/10.1016/j.chemgeo.2024.122318
Received 7 May 2024; Received in revised form 8 August 2024; Accepted 9 August 2024
Available online 10 August 2024

the liquid-vapor homogenization temperature (T_h). Since the thermodynamic properties of the system are relatively well known, this proxy method does not rely on empirical calibrations or assumptions about equilibrium conditions that commonly represent a major source of uncertainty of other paleothermometers. Fluid inclusions in halite, however, are typically in a single-phase liquid state at room temperature, and thus, nucleation of a vapor bubble is a mandatory precondition for measuring the temperature of liquid-vapor homogenization. Under negative internal pressures, single-phase liquid inclusions are metastable, and, given sufficient time, vapor bubbles will nucleate spontaneously in the metastable liquid. The rate at which this process occurs is proportional to the magnitude of the negative pressure applied to the liquid (Church, 2002). Increasing the magnitude of negative pressure in liquids has been achieved by isochoric cooling, application of centrifugal force, and application of focused acoustic waves (Caupin and Herbert, 2006; Herbert et al., 2006; Davitt et al., 2010; Arvengas et al., 2011; Caupin, 2023). Storage of halite samples at −10 to −20 °C in a refrigerator/freezer has previously been used to provoke spontaneous nucleation of the vapor bubble (Roberts and Spencer, 1995; Lowenstein et al., 1998; Benison and Goldstein, 1999; Goldstein, 2001; Guillerm et al., 2020). Upon cooling, the fluid pressure in the inclusion evolves along a pseudo-isochoric *p-T* trajectory, passing from a stable into a metastable liquid state, where pressure becomes negative, *i.e.* the liquid phase is under tensile stress, and if that tensile stress becomes large enough, a vapor bubble may nucleate spontaneously (Fig. 1).

Previous studies of halite fluid inclusions have noted issues in the reproducibility and precision of the T_h measurements and reported a wide scatter of temperature data, displaying a characteristic low-temperature tail (McCulloch, 1959; Roedder, 1984; Lowenstein et al., 1998; Meng et al., 2011; Rigaudier et al., 2011; Speranza et al., 2013; Zhang et al., 2015; Zhang et al., 2017; Guillerm et al., 2020). The reason for these wide temperature distributions (~10–50 °C scatter) is the high negative pressure required to provoke spontaneous bubble nucleation and its effect on a soft halite host. Plastic deformation of the inclusion walls causes a decrease of the inclusion volume, resulting in a higher fluid density and thus, lower homogenization temperature. The resultant volume change of the inclusions is related to the internal tensile stress, the size of the inclusion, and its proximity to nearby inclusions and crystal surfaces (Guillerm et al., 2020).

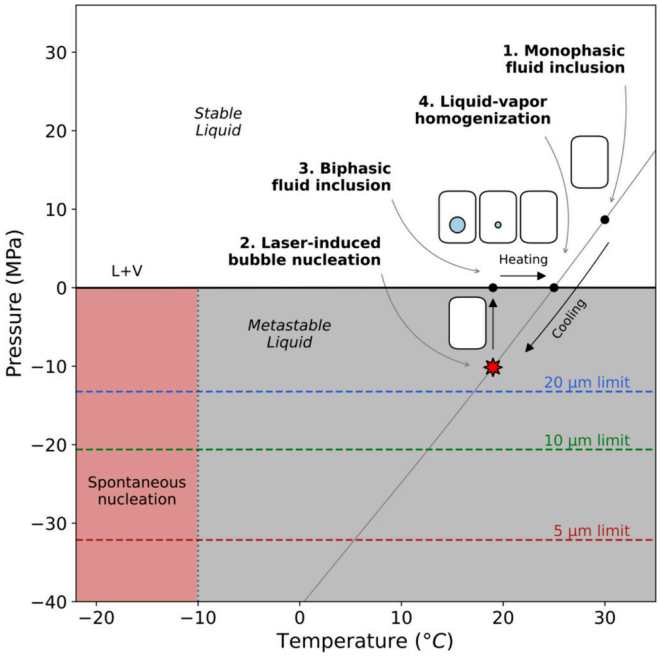

Fig. 1. Pressure-temperature (*p-T*) projection of the NaCl-H_2O system at halite saturation (liquid inclusion in halite) showing the stable liquid field, the metastable liquid field (shaded gray) below the liquid-vapor equilibrium curve (L + V), and the *p-T* path of a hypothetical FI with a nominal T_h^∞ of 25.0 °C (ρ = 1.20 g/cm^3) during NA-microthermometric analysis (modified from Krüger et al., 2011; Guillerm et al., 2020; Olson et al., 2023). Brine inclusions do not exhibit a density-maximum and can therefore reach high negative pressure upon cooling (pink shading) to promote spontaneous nucleation of a vapor bubble. Colored dashed lines indicate yield stress pressure limits for different inclusion sizes (Guillerm et al., 2020). Cooling a FI beyond its yield stress pressure limit results in plastic deformation of the inclusion walls. NA microthermometry can stimulate vapor bubble nucleation before the inclusion exceeds the yield stress limit. (For interpretation of the references to colour in this figure legend, the reader is referred to the web version of this article.)

Here, it is worth mentioning an alternative, purely physical approach to determine halite formation temperatures by means of Brillouin spectroscopy, which was proposed by El Mekki-Azouzi et al. (2015). The method makes use of the speed of sound measured in fluid inclusions as a function of temperature and pressure. The measurements are performed in a relatively narrow temperature range both in the single-phase liquid along the (pseudo-)isochore and subsequently along the liquid-vapor equilibrium curve (after overheating and stretching the inclusions to generate the vapor bubble). The temperature T_x at which the two sound-velocity curves intersect determines the density of the solution and is equivalent to the liquid-vapor homogenization temperature T_h^∞ that could be measured in a hypothetical infinitely large inclusion by microthermometry (*cf.* section 2.1.4, *Data processing*).

In this study, we employ a more refined, simple, and yet highly efficient technique to overcome metastable phase states in fluid inclusions by means of single ultra-short laser pulses from a femtosecond laser (Fig. 2) (Krüger et al., 2007). This method, referred to as nucleation-assisted (NA) microthermometry, allows for bubble nucleation in pre-selected fluid inclusions under simultaneous visual observation at temperatures just slightly below the expected homogenization temperature. NA microthermometry has previously been employed for paleo-temperature reconstructions using fluid inclusions in stalagmites (Krüger et al., 2011; Meckler et al., 2015; Løland et al., 2022) and for other fluid inclusion studies involving shallow-subsurface mineralization of various host crystals (Krüger et al., 2013; Gilg et al., 2014; Koltai et al., 2024).

The objective of the present study is to explore the precision and accuracy of NA microthermometry applied, for the first time, to fluid inclusions in halite using lab-grown crystals (i). We further evaluate the method using modern varved halites from the Dead Sea with reference to an instrumental water temperature record (ii). Finally, we then apply this method to reconstruct temperatures from Late Pleistocene and Holocene halites from a Death Valley sediment core, covering the last glacial Termination, for which temperature is not independently constrained (iii).

2. Materials and methods

2.1. Methods

2.1.1. Experimental Setup

NA microthermometry was performed in the fluid inclusion lab at the University of Bergen on an Olympus BX53 microscope, equipped with a 100× LWD objective lens (Olympus LMPLFLN), a Linkam THMS600 heating-cooling stage, and a pco.edge 3.1 sCMOS camera. The heating-cooling stage was calibrated with synthetic H_2O and H_2O-CO_2 fluid inclusion standards, using the triple point of water (0.0 °C) and the critical temperature of CO_2 in the H_2O-CO_2 system (31.4 °C; Morrison, 1981). Temperature accuracy was ±0.1 °C. An amplified TI:Sapphire femtosecond laser system (CPA 2101, Clark MXR, Inc.), providing ultra-short laser pulses of *ca.* 200 fs (1 fs = 10^{-15} s), was used to stimulate vapor bubble nucleation in metastable liquid inclusions. Femtosecond laser pulses have very high peak power, but due to their ultra-short duration, they deposit only very little energy into the sample. Sub-microscopic

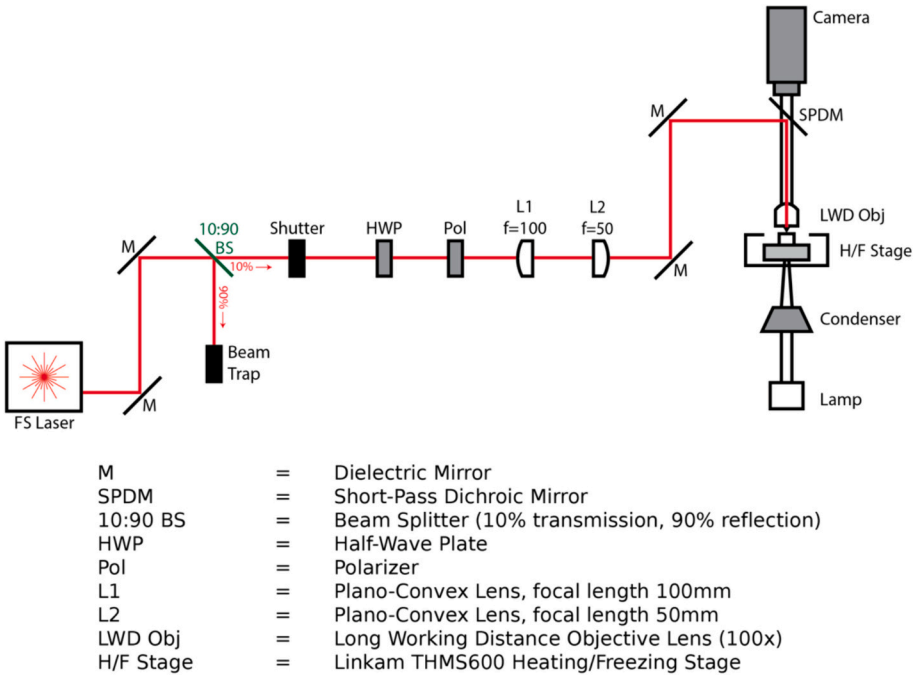

Fig. 2. Schematic diagram of the analytical setup used for NA microthermometry. The TI:Sapphire femtosecond laser system (CPA series 2101, Clark MXR, Inc.) is interfaced to an Olympus BX53 microscope using a series of mirrors, a 10:90 beam splitter, as well as a rotatable half-wave plate combined with a fixed Glan laser polarizer to attenuate and fine-tune the energy of the laser pulse, and a 2:1 beam telescope consisting of two plano-convex lenses with 100 and 50 mm focal length, respectively, to reduce the beam diameter. A short-pass dichroic mirror is used to couple the laser beam into the microscope light path. The microscope is equipped with a 100× LWD objective, a Linkam THMS600 heating/cooling stage and a digital camera. The pulse trigger and beam shutter are controlled via a custom-made remote-control panel.

ablation, induced by single laser pulses focused on the surface of an inclusion, produces a pressure wave (a compression-rarefaction wave) that propagates through the inclusion and may provoke nucleation of the vapor bubble or other metastable absent phases like salt crystals or salt hydrates (Krüger et al., 2007). The laser beam was directed to the microscope via mirrors through a 10:90 beam splitter, a rotatable half-wave plate and fixed Glan laser polarizer, and a 2:1 beam telescope to match the beam diameter to the back aperture of the 100× objective. Finally, the 775 nm laser beam was coupled into the microscope light path via a dual port intermediate tube (Olympus U-DP) equipped with a short-pass dichroic beam splitter (675DCSPXR, Omega Optical). A schematic representation of the setup is shown in Fig. 2. The output power of the emitted laser light was reduced to about 20 mW (at 1 kHz repetition rate) and then further attenuated by passing through the 10:90 beam splitter. For stimulating vapor bubble nucleation, the laser was operated in single pulse mode, and to avoid damaging the inclusions, the pulse energy was further reduced by means of the rotatable half-wave plate and the fixed polarizer, which allowed fine-tuning of the pulse energy to a level at or slightly above the threshold required for bubble nucleation but below the threshold of visible ablation (Krüger et al., 2007).

2.1.2. Sample preparation and selection of fluid inclusions

Halite crystals or fragments, about ~1–5 mm side length (*i.e.* large enough to be manipulated and analyzed, but small enough to fit on the heating/cooling stage), were cleaved with a razor blade to a thickness of <500 μm for microthermometric analyses of the fluid inclusions on the microscope heating/cooling stage (Fig. 3b). Primary fluid inclusions, *i.e.* inclusions that formed during halite precipitation, are arranged along former crystal surfaces and evince the characteristic growth zonation of the halite crystals shown in Fig. 4c and 5b (*e.g.* Goldstein and Reynolds, 1994). Following Guillerm et al. (2020), we selected inclusions that were sufficiently small ($\lesssim$ 30 μm side lengths, or 30^3 μm^3 volume) and that were distant from other inclusions and from the crystal surface (>2 fluid inclusion-radii from the center of each fluid inclusion) to minimize potential plastic deformation of the inclusion walls during microthermometric measurements (Fig. 3c).

2.1.3. Analytical procedure

Laser-induced nucleation of the vapor bubble requires that the fluid inclusions are in a metastable liquid state, *i.e.* at a temperature below the liquid-vapor homogenization temperature (T_h) that is unknown *a priori*. The geological context of the halite samples provides information about whether homogenization temperatures are above or below the ambient lab temperature. In practice, some trial-and-error is needed to find an adequate nucleation temperature, T_n, for laser-induced bubble formation. However, a temperature difference of <10 °C between T_n and T_h is required to avoid high negative liquid pressures that may produce plastic deformation to the inclusion walls. Photomicrographs of the cubiform inclusions were taken to document their dimensions (side lengths) for calculating the volume of the inclusions. Two of three principal axis side-lengths are observable under planar view, and the third dimension (depth) is calculated as the geometric mean of the two observable side-lengths.

Following laser-induced bubble nucleation, measurements of T_h were performed using protocols described by Goldstein and Reynolds (1994), which ensure that samples and the heating/cooling stage are in thermal equilibrium when the temperature approaches T_h. In order to ensure accurate measurement of T_h to within 0.1 °C, a slow heating rate (< 1 °C/min) was applied when approaching bubble collapse. In most inclusions, the collapse of the vapor bubble could be visually observed. In cases where the collapse of the vapor bubble could not be directly observed, a temperature cycling procedure was applied to determine T_h accurately (Goldstein and Reynolds, 1994). Following Fall et al. (2009), the observed (measured) homogenization temperature, is called "$T_{h,obs}$". In general, we analyzed between 40 and 60 fluid inclusions in each sample when possible, in order to obtain sound statistics, and measurements were replicated to ensure reproducibility.

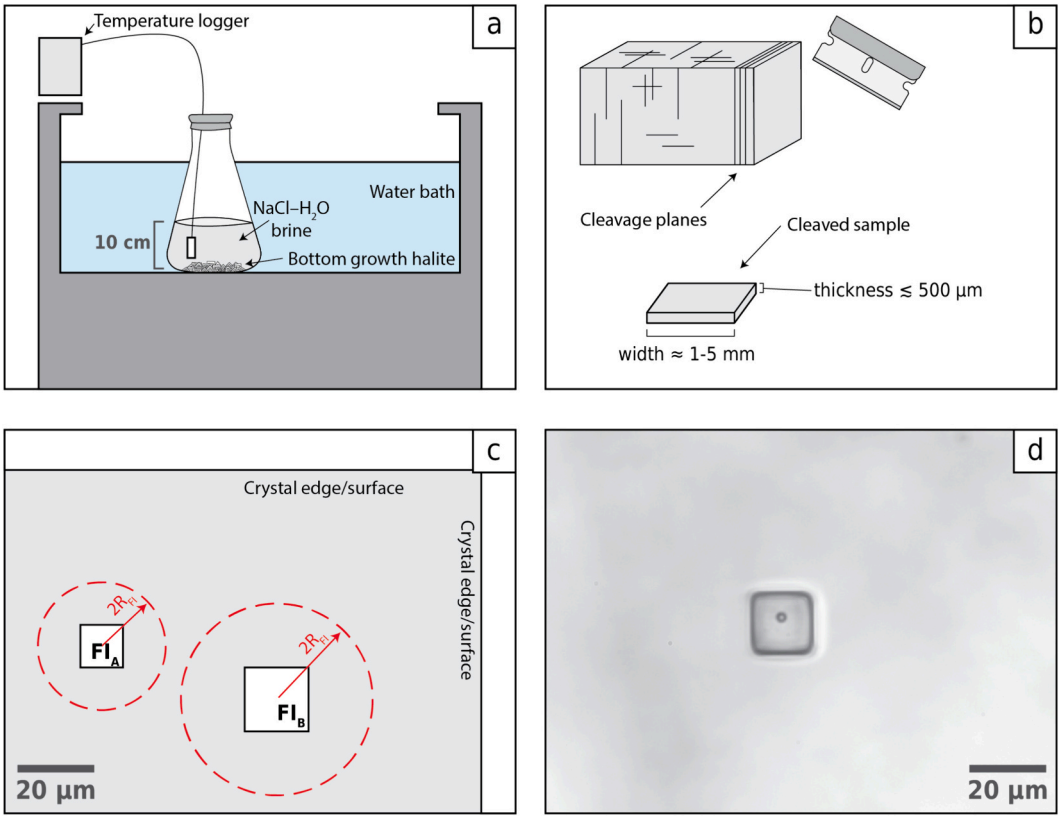

Fig. 3. Sample preparation and selection criteria for halite analyzed in this study. (a) Diagram of halite grown in a water bath under controlled conditions. NaCl-saturated brine in a covered Erlenmeyer flask was submerged in the water bath, monitored via a temperature logger. Halite crystals precipitated at the bottom of the flask over a 6-month period until they were large enough (~1-5 mm side length) to be analyzed. (b) Illustration showing ideal crystal dimensions, 1–5 mm side length (s) and ≲ 500 µm thickness, split along cleavage planes with a razor blade. (c) Diagram showing ideal fluid inclusion geometry and location within crystals, relative to crystal edges and other fluid inclusions. Ideal inclusions for analysis are small (≲ 20 µm side length), isolated from one another (at least two FI-radii, $2R_{FI}$, apart from one another), and not in close proximity to crystal edges/surfaces (criteria from Guillerm et al., 2020). (d) inclusion analyzed from lab-grown halite samples showing ideal dimensions and isolation from other inclusions/crystal edges.

2.1.4. Data processing

The measured homogenization temperature $T_{h,obs}$ depends not only on the density of the fluid but also on the volume of the inclusion (*cf.* Fall et al., 2009; Marti et al., 2012). In practice this means that small inclusions yield lower $T_{h,obs}$ values than large inclusions with the same fluid density. The reason for this is the so-called Laplace pressure, *i.e.* the pressure difference Δp between the liquid and the vapor phase that arises due to the surface tension at the liquid-gas interface of the vapor bubble; this pressure difference is described by the Young-Laplace equation:

$$\Delta p = 2\sigma/r \quad (1)$$

where σ is the surface tension and r is the radius of the vapor bubble. In order to obtain the correct density of the fluid, a "Laplace" pressure correction term ΔT_L needs to be applied to $T_{h,obs}$ that takes the effect of surface tension on liquid-vapor homogenization into account (Fig. 6). This is done by calculating T_h^∞, the homogenization temperature of a hypothetical, infinitely large inclusion of the same density. As the bubble radius in this hypothetical inclusion approaches infinity, Δp becomes zero and hence $T_{h,obs}$ is not affected by the surface tension and would equal T_h^∞. The calculations of T_h^∞ are based on the measured $T_{h,obs}$ and the inclusion volume, derived from the side lengths of the cubiform halite fluid inclusions, using the numerical formulation proposed by Caupin (2022), which, in contrast to the pure water model proposed by Marti et al. (2012), can be applied to aqueous salt solutions (see *supplementary material*). In addition, the calculations involve the multi-electrolyte surface tension equation of Dutcher et al. (2010), the multi-electrolyte equation of state of Al Ghafri et al. (2012, 2013), and the halite equation of state of Driesner (2007) for the thermal expansion of the halite host.

If the fluid inclusions formed at atmospheric pressure, T_h^∞ can ideally be considered equal to the formation temperatures T_f, as would be the case for lab-grown halite crystals. In reality, however, T_h^∞ values of coeval inclusions typically display significant scatter with unimodal Gaussian-like distributions, and we consider the mean value T_{havg}^∞ as the best approximation of the halite formation temperature ($T_f \equiv T_{havg}^\infty$). If, however, the inclusions formed at the bottom of a lake, an additional temperature correction term is needed to take account of the hydrostatic pressure of the overlaying water column ($T_f = T_{havg}^\infty + \Delta T_p$) (Fig. 6). This pressure correction ΔT_p is based on the slope of the pseudo-isochoric p-T trajectory of the inclusion and requires an estimate of the lake depth. For the Dead Sea samples, assuming 35 m water depth and modern Dead Sea chemistry from Krumgalz et al. (2000), we calculated $\Delta T_p = 0.37$ °C; for the Death Valley samples, assuming a 90 m water column and Death Valley brine chemistry from Li (1996), we calculated $\Delta T_p = 0.69$ °C (see *supplementary material*).

For each halite sample measured in this study, the mean value (μ) of the T_h^∞ (or $T_h^\infty + \Delta T_p$) distribution, standard deviation (σ), and standard error of the mean (SEM) were estimated by means of bootstrap resampling (100,000 iterations). Original samples sizes, *i.e.* the number of inclusions analyzed in each sample, were typically >40. We apply a conservative 4 median absolute deviation (MAD) threshold for the robust detection of outliers prior to calculation of sample statistics (Hampel, 1974). Histograms for each individual halite sample were used to assess normality and to detect signs of skew in the distribution of

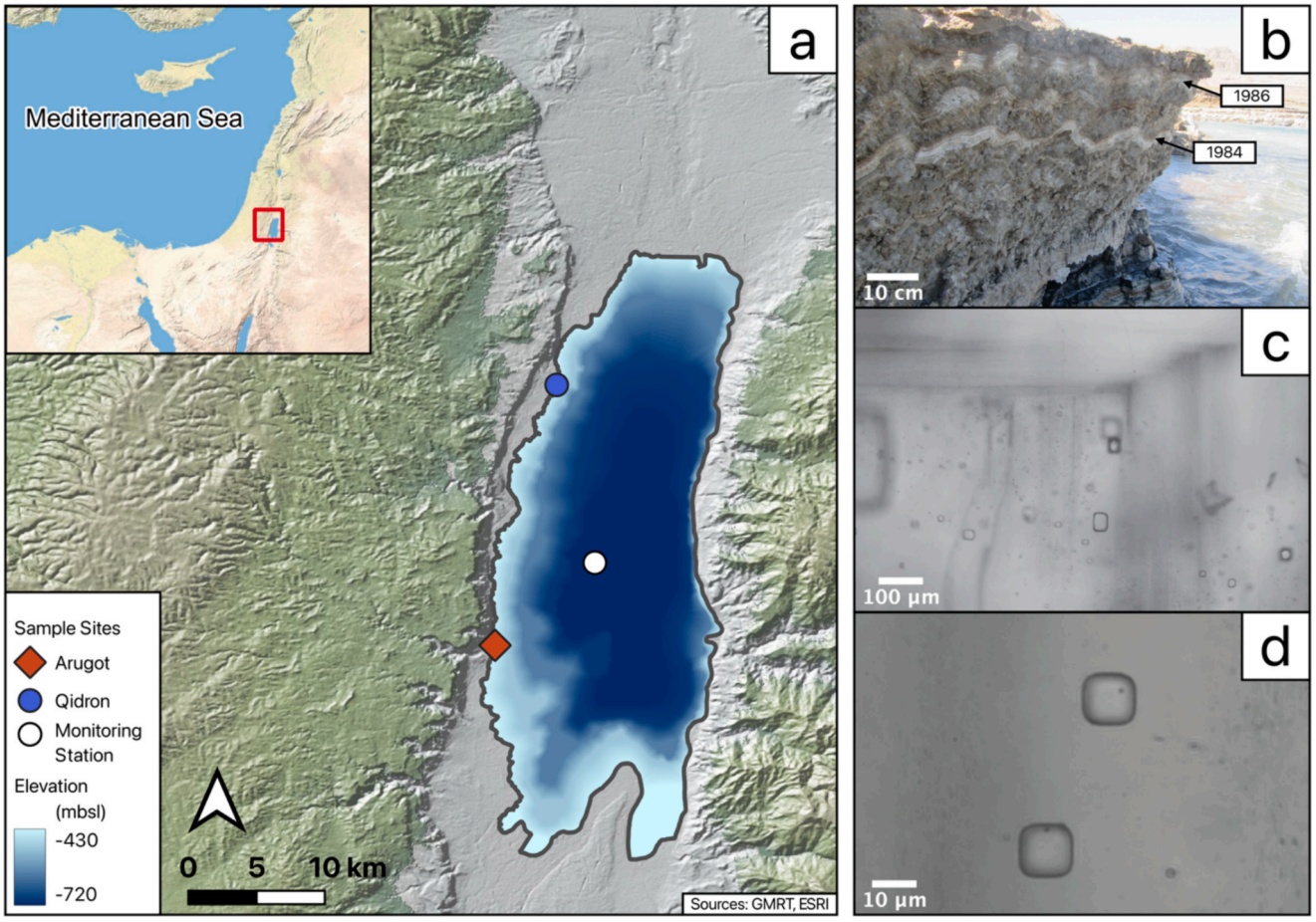

Fig. 4. (a) Map of Dead Sea showing halite sample locations and field-monitoring station from Anati and Stiller (1991). (b) Qidron outcrop showing halite varves annotated with year of deposition. (c) and (d) Fluid inclusions in halite precipitated in 1986 from the Qidron outcrop. (d) Close-up photomicrograph of fluid inclusions with vapor bubbles nucleated with a single femtosecond laser pulse.

temperatures. In addition, T_h^{∞} vs. fluid inclusion-size scatter plots were used to test for potential plastic deformation of the inclusions due to internal tensile stress that would become manifest in a negative correlation of the two parameters. For temperature reconstructions, 2SEM uncertainties were estimated for each sample, representing approximately 95% confidence intervals for the mean T_h^{∞}/T_f.

2.2. Halite samples

2.2.1. Study 1: Lab-grown halites

Synthetic halite crystals were grown in the lab under controlled temperature conditions (Fig. 3a). A flask (500 ml) with 10 cm of halite-saturated NaCl-H_2O brine was submerged at 25 °C in a temperature-controlled circulating water bath (VWR 1150S). The flask was covered with a thin perforated sheet of aluminum foil to reduce evaporation, allowing crystals to grow slowly at the bottom of the brine. Brine temperature was measured at 5-min intervals using a HOBO MX2304 temperature logger, placed directly into the 500 ml flask of solution. The reported accuracy of the data logger is ±0.2 °C, and the brine temperature monitored over the entire growth period was 25.06 ± 0.03 °C (1 SD; range = 24.94–25.15 °C); we report the brine temperature range with combined uncertainty for the duration of halite growth as 24.74–25.35 °C. Crystals grew over a 6-month period until they were large enough 1–5 mm) with sufficient fluid inclusions to be analyzed with microthermometry.

2.2.2. Case Study 2: 1980s varved halite from the Dead Sea

Modern halite samples from the Dead Sea were collected along the western shoreline during a field campaign in February 2023. The halites grew between 1983 and 1987, a period over which monitoring data of lake bottom-water temperatures (BWT) is available (Fig. 4) (Anati and Stiller, 1991). Due to continuous recession of the lake level since the late 1970s, halite began to precipitate in the central part of the Dead Sea at a rate of ~0.1 m/yr (Lensky et al., 2005) from 1979 onwards (Steinhorn, 1983). The varved halite samples show seasonal alternations of coarse bottom-growth crystals precipitated during the summer season (approx. March to October) and fine cumulates that precipitated in the water column during winter (approx. November to February) (Sirota et al., 2017, 2021) (Fig. 4b). 5 varves, covering the period from 1983 to 1987, were sampled at Arugot, and 2 varves, precipitated in 1984 and 1986, were sampled at Qidron (Fig. 4a). The two outcrops are located 437 m below sea level, corresponding to a lake depth in the 1980s of ~35 m. The Dead Sea experienced a lake level recession of ~1 m/yr since the 1980s (Lensky et al., 2005); thus, the outcrops were under water until a few months before sampling in 2023. We estimate that the outcropping halite samples were subjected to fluctuating brine temperatures ranging between ~15–35 °C; as a precaution against potential alterations of the fluid inclusions caused by the extreme summer heat, ~50 cm was scraped off the outcrop surface before collecting the samples.

The fluid inclusions in the halite crystals are expected to record water temperatures from the hypolimnion (below the thermocline). We compare them with temperatures from the center of the Dead Sea measured between 1983 and 1987 at 100–320 m water depth (Anati and Stiller, 1991). Lateral variability of hypolimnion temperatures across the basin is generally low, up to 0.5 °C in July (Lensky et al., 2013). Temperatures ranged between 21.8 and 23.1 °C in the 1980s, and the

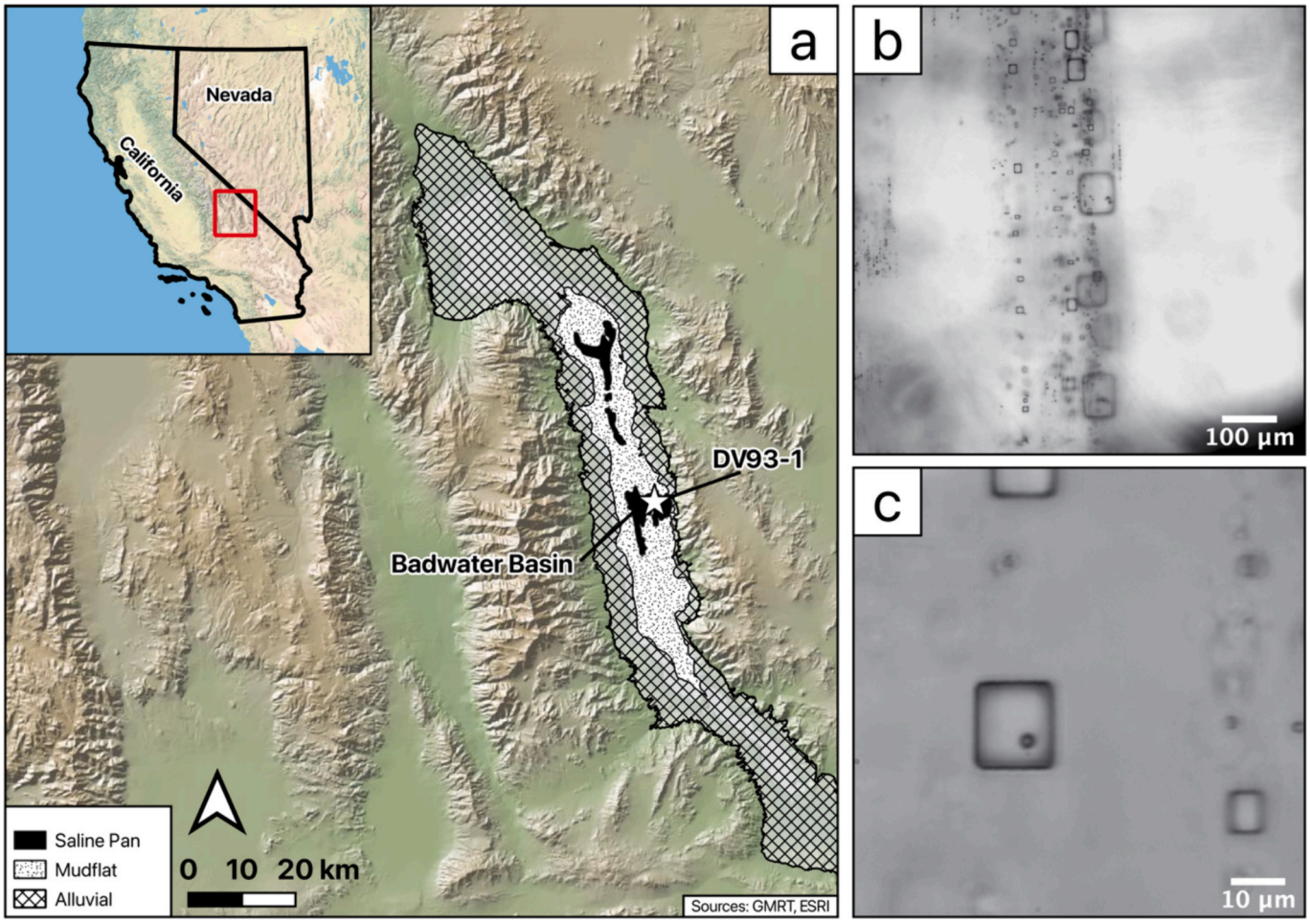

Fig. 5. (a) Map of Death Valley, CA, showing modern depositional environments, Badwater Basin, and location of core DV93–1. (b) Thin section photomicrograph of fluid inclusion band in crystal of halite, core DV93–1 depth of 8.7 m. (c) Close-up photomicrograph of a fluid inclusion with vapor bubble nucleated using a femtosecond laser, core DV93–1, depth of 8.7 m.

average vertical gradient generally did not exceed 0.7 °C, with minimum and maximum temperatures occurring at the top and the bottom of the profile, respectively (Gertman and Hecht, 2002; Arnon et al., 2016). Analysis of internal wave propagation within the modern Dead Sea indicates that oscillations in thermocline depth of ±5 m or more may be observed for brief periods (Arnon et al., 2019). We estimate that these oscillations could potentially result in temperature excursions of up to a few degrees from average bottom water temperatures (see *supplementary material*). Maximum bottom water temperature is generally observed at the end of the year (November–December), due to seasonal overturning and mixing of the water column, rather than during peak-summer through fall (July–September), during which time the water column remains stratified (Arnon et al., 2016).

Halite crystals used for fluid inclusion analysis were sampled from the base and from the top of coarse bottom-grown halite layers from Arugot and Qidron outcrops, and one additional sample was taken from the middle of varve Arugot 1984. Fine cumulate halite crystals that form during winter were excluded from this study due to uncertainty regarding where in the water column they precipitated. Temperatures reconstructed from the base and top of the bottom-grown halite sequence are expected to reflect water temperatures during March and October, respectively, with an estimated uncertainty of ± ~1 month.

2.2.3. *Case Study 3: Pleistocene halite from basin-center Death Valley core*

Two halite samples from a 185.5 m long sediment core (DV93–1) from Badwater basin, Death Valley (Fig. 5), one late Pleistocene and the other Holocene, were analyzed in this study and compared to previously published results derived by classical microthermometry (Lowenstein et al., 1998). For this re-analysis, halite samples were selected at the same core depths as those used in the forerunner study, 8.7 m and 15.8 m. Sedimentary and petrographic features (upward competitive growth) indicate halite crystallization at the bottom of a perennial lake with an estimated water depth of, at most, ~90 m (Lowenstein and Hardie, 1985; Casas and Lowenstein, 1989; Li et al., 1996; Lowenstein et al., 1998). According to the revised age model for core DV93–1 (Lowenstein et al., 2024), sample DV 15–1 from 15.8 m depth is 26.3 ± 4.8 ka, corresponding to the Last Glacial Maximum (LGM); sample DV 10–3 from 8.7 m depth is early Holocene in age (10.0 ± 3.9 ka).

3. Results

3.1. *Case Study 1: lab-grown halite*

In total, 50 fluid inclusions were selected from four halite crystals for microthermometric measurements. The distributions of measured $T_{h,obs}$ (Fig. 7a) and Laplace-corrected T_h^{∞} (Fig. 7b) from lab-grown halite are Gaussian-like and roughly unimodal. The mean of the T_h^{∞} distribution yields a formation temperature T_f of 25.3 ± 0.2 °C (2SEM), which is slightly higher than, but still in agreement with, the actual brine temperature of 25.05 ± 0.3 °C measured during crystal growth. The scatter of T_h^{∞} (23.1–27.4 °C, Δ = 4.3 °C, σ = 0.8 °C), in contrast, is one order of magnitude larger than the variability of the brine temperature

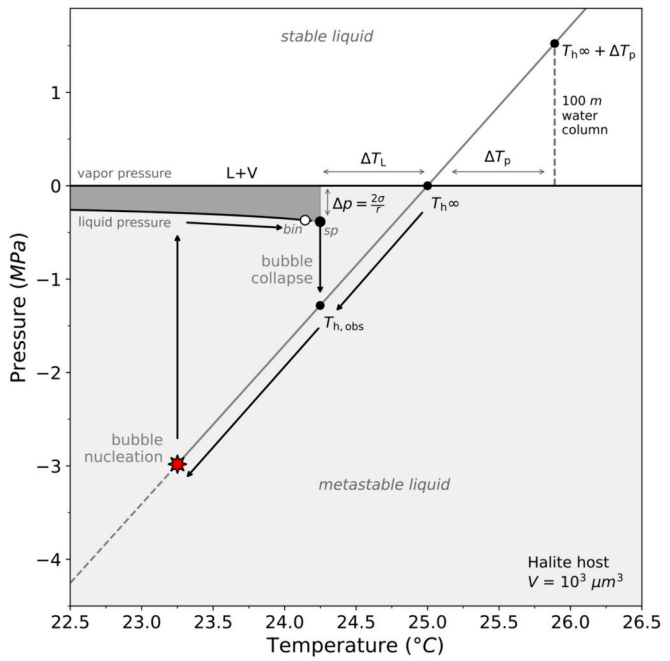

Fig. 6. *p–T* diagram of NaCl-saturated water illustrating the change in liquid pressure for single- and two-phase states as a function of temperature for a 1000 μm^3 inclusion with T_h^∞ of 25.0 °C, as well as the Laplace- and hydrostatic-pressure corrections for an inclusion in halite formed at 100 m water depth (Modified from Krüger et al., 2011). Upon vapor bubble nucleation, liquid pressure increases but remains negative (tension), while vapor pressure is close to saturation pressure, resulting in a pressure difference Δp (Laplace pressure). Upon heating, the vapor bubble becomes smaller and Δp increases according to the Young–Laplace equation (as shown). At temperature T_{bin}, the stable two-phase state becomes metastable (*binodal*) and finally mechanically unstable at T_{sp} (*spinodal*). Bubble collapse is observed at $T_{h,obs}$, between T_{bin} and T_{sp}, so a Laplace correction term ΔT_L is needed to account for the difference between $T_{h,obs}$ and T_h^∞. If the inclusion was trapped at the bottom of a water column, a hydrostatic pressure correction ΔT_p is needed to account for the difference between saturation (T_h^∞) and hydrostatic pressure.

(24.94–25.15 °C, Δ = 0.21 °C, σ = 0.03 °C). The absence of a correlation between T_h^∞ and inclusion size, illustrated in Fig. 7c, indicates that the scatter of the T_h^∞ values is not related to plastic deformation caused by tensile stress occurring in the metastable liquid state of the brine.

3.2. Case study 2: 1980s varved halite from the Dead Sea

Reconstructed formation temperatures of 15 bottom-grown halite samples covering the period from 1983 to 1987 are shown in Fig. 8, along with instrumental lake temperatures recorded during the same period (Anati and Stiller, 1991). Individual sample histograms and T_h^∞-fluid inclusion size plots for each sampled horizon and outcrop are shown in Fig. 9. Between 39 and 51 inclusions were analyzed in at least two different crystals at each sample position, except one sample (Arugot 1984 top), for which 21 inclusions were analyzed from two subsamples. The scatter of the T_h^∞ values varies for the different samples, with standard deviations ranging from 0.6 to 1.7 °C and an average value of 1.2 °C. For all samples, the median T_h^∞ is within two standard errors of the mean (2SEM), indicating that the estimated average T_h^∞ is robust.

Estimated formation temperatures T_f include a correction for hydrostatic pressure at water depths of 35 m depth ($T_{h,avg}^\infty$ + 0.37 °C) with 2 SEM ranging between 0.2 and 0.5 °C. The weighted average T_f from the 15 samples is 22.1 ± 1.2 °C (1 SD); the average instrumental BWT temperature during the time of halite precipitation was 22.2 ± 0.4 °C (1 SD). The T_f time-series qualitatively captures a long-term warming trend of the Dead Sea during the years 1983–1987, with an average warming of 0.4 °C/yr, consistent with the instrumental BWT warming trend of 0.15 °C/yr (Fig. 8). The ΔT_f between the base and top of varves 2, 3, and 4 (1984, 1985, and 1986) captures an average summer warming of the Dead Sea by 1.2 °C (range = 0.9–1.6 °C).

3.3. Case study 3: Pleistocene halites from basin-center Death Valley core

The results from the two Death Valley halite samples are shown in Fig. 10 and contrasted with previous results reported by Lowenstein et al. (1998). For the late Pleistocene sample DV 15–1 (Fig. 10b,d), inclusions from two halite chips were analyzed; for the Holocene sample DV 10–3 (Fig. 10a,c), inclusions from three halite chips were analyzed. Both samples display narrow unimodal distributions of the pressure-corrected (ΔT_p = +0.69 °C) temperatures. In contrast to these narrow, Gaussian-like distributions, the distributions obtained with classical microthermometry, involving (pseudo-)isochoric cooling to provoke bubble nucleation are random, each with a temperature range of >20 °C (Fig. 10a,b; gray histograms). At the time, Lowenstein et al. (1998) utilized the maximum observed homogenization temperature, $T_{h,obs(max)}$, to estimate water temperature, and reported temperatures of 30 °C for DV 10–3 and 23 °C for DV 15–1, though without quantifiable uncertainty. The new estimated formation temperatures for these samples from NA microthermometry are consistent with the previous $T_{h,obs(max)}$ estimates, but it should be noted that the reliability of $T_{h,obs(max)}$ is dependent on large sample sizes and could easily be biased to lower temperatures.

The late Pleistocene sample DV 15–1 (26.3 ± 4.8 ka) yields a formation temperature T_f of 24.3 ± 0.2 °C (2SEM) with a standard deviation (σ) of 0.8 °C (n = 46). The Holocene sample DV 10–3 (10.0 ± 3.9 ka), on the other hand, yields a T_f of 28.7 ± 0.4 °C (2SEM) and a larger σ of 1.4 °C (n = 62). The results indicate warming of lake bottom water of 4.4 ± 0.45 °C between deposition of these two halites, consistent with the interpretation of deglacial warming across the last glacial Termination (Osman et al., 2021).

4. Discussion

The results from the three case studies are used to discuss a series of factors impacting the accuracy and precision of lake temperature reconstructions derived from halite fluid inclusions by NA microthermometry. We emphasize that halite, due its low hardness and ease of plastic deformation as well its high solubility, is generally considered a difficult host mineral for fluid inclusion microthermometry. Moreover, the application of halite fluid inclusions as an archive of past lake water temperatures makes high demands on the integrity of the preserved temperature information and on the precision and accuracy of the analytical method employed to attain this information. Here we demonstrate that it is indeed possible to achieve a high degree of accuracy and precision using NA microthermometry on fluid inclusions in halite.

4.1. Analytical accuracy and precision

First, we assess the accuracy and precision of T_h^∞ with respect to analytical error. The accuracy of $T_{h,obs}$ measurements is, on the basis of the temperature calibration of the heating-cooling stage, better than ±0.1 °C for the temperature range of interest. Replicate measurements of individual inclusions are typically reproducible to within ±0.1 °C (precision). Analyses were performed with a metal lid over the sample on the heating/cooling stage, ensuring a low thermal gradient in the sample chamber. Furthermore, slow heating rates (<1°/min) were applied as inclusions approached $T_{h,obs}$, resulting in more accurate measurement of $T_{h,obs}$ (within 0.1 °C). We performed replicate $T_{h,obs}$ measurements for most inclusions to test precision and reproducibility. All replicate measurements made on lab-grown halites were

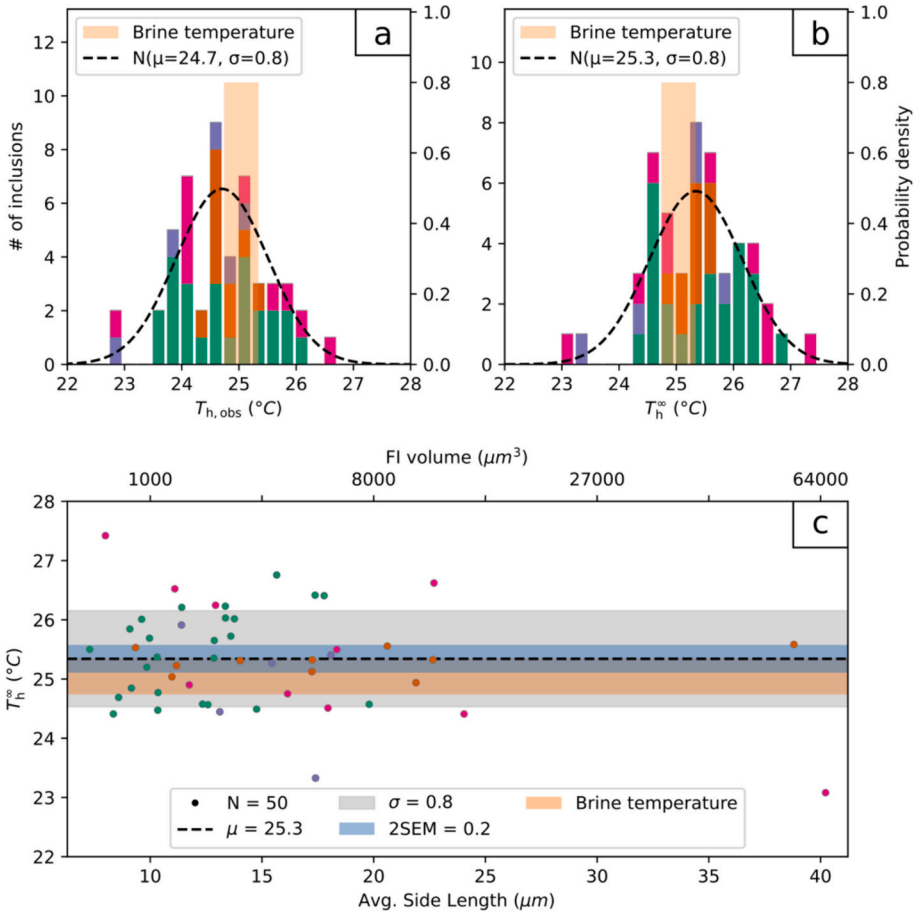

Fig. 7. (a-b) Histograms of homogenization temperatures from halite grown in a water bath at 25.05 ± 0.3 °C, shown (a) before ($T_{h,}$obs) and (b) after surface tension correction (T_h^∞). Colors represent individual crystals. Gaussian "Normal" distributions (black dashed curves) were fitted to the sample by bootstrapping the mean (μ) and standard deviation (σ). The brine temperature is shown by the orange rectangle. (c) Plot of T_h^∞ vs. average inclusion side length for all fluid inclusions. Colors represent individual crystals. The light blue error bar represents two standard errors of the mean (2SEM). The gray error bar represents standard deviation from the mean (σ). The brine temperature is shown in orange. (For interpretation of the references to colour in this figure legend, the reader is referred to the web version of this article.)

reproducible to 0.1 °C (n = 38), which is within the range of the temperature stability of the heating-colling stage (±0.05 °C), 97% of measurements made on Dead Sea halites were reproducible to 0.2 °C with a mean difference between first and second measurements of 0.15 °C (n = 353), and 98% of measurements made on Death Valley halites were reproducible to 0.2 °C with a mean difference between measurements of 0.02 °C (n = 108).

The accuracy of the Laplace correction ΔT_L for calculating T_h^∞ depends on the accuracy of the employed equations of state (EoS) and on the accuracy of the volume determination of the inclusions. Since ΔT_L increases with decreasing inclusion volume, the impact of relative volume errors on the resulting ΔT_L becomes larger for small inclusions and underestimations of volume than for large inclusions and volume overestimations, respectively. The sensitivity of ΔT_L to relative volume uncertainties of up to ±50% is illustrated in Fig. 11a. For inclusions with average side lengths between 5 and 50 μm (volumes of 125 and 125,000 μm^3), moderate volume uncertainty (20–50% of estimated volume) results in a small uncertainty on the Laplace correction (~0.1–0.2 °C).

Under visual observation, two of the three dimensions (side lengths) of cubiform halite inclusions are easily measured, but uncertainty lies in the measurement of the third dimension (depth). For inclusions in this study, we estimated the third dimension as the average of the two measured side-lengths. This third-dimension estimate is the principal source of error in the Laplace corrections. An alternative approach for calculating inclusion volume uses $T_{h,obs}$, the radius of the spherical vapor bubble at known temperature, and thermodynamic modeling (Krüger et al., 2011; Marti et al., 2012; Løland et al., 2022). However, this method is time-consuming and can also lead to errors given the small size of the bubbles, the focus position of the bubble images, and human error in the measurement of the vapor bubble size.

There is an additional inherent uncertainty related to the ambiguity of $T_{h,obs}$ within a metastable liquid-vapor two-phase state: bubble collapse must take place between T_{bin} (*bubble binodal*) and T_{sp} (*bubble spinodal*), but where exactly the bubble collapses relative to T_{bin} and T_{sp} is unpredictable (Marti et al., 2012). For fluid inclusion volumes of 30^3 and 5^3 μm^3, the additional uncertainty on T_h^∞ is ±0.02 to ±0.09 °C, respectively (see Fig. 11b). When these errors are propagated into sample statistics by means of Monte Carlo simulations, the contribution to overall error on the sample mean is generally negligible.

4.2. *Accuracy and precision of reconstructed T_f values*

In the present study, we evaluated the accuracy and precision of reconstructed halite formation temperatures T_f obtained with NA microthermometry by means of the synthetic, lab-grown halite crystals (case study 1), and modern halite samples from the Dead Sea (case study 2) that precipitated at known, well-constrained bottom water temperatures. While the temperatures measured from Pleistocene-Holocene halites from Death Valley (case study 3) can't be tested for accuracy without an independent temperature proxy, the scatter observed from

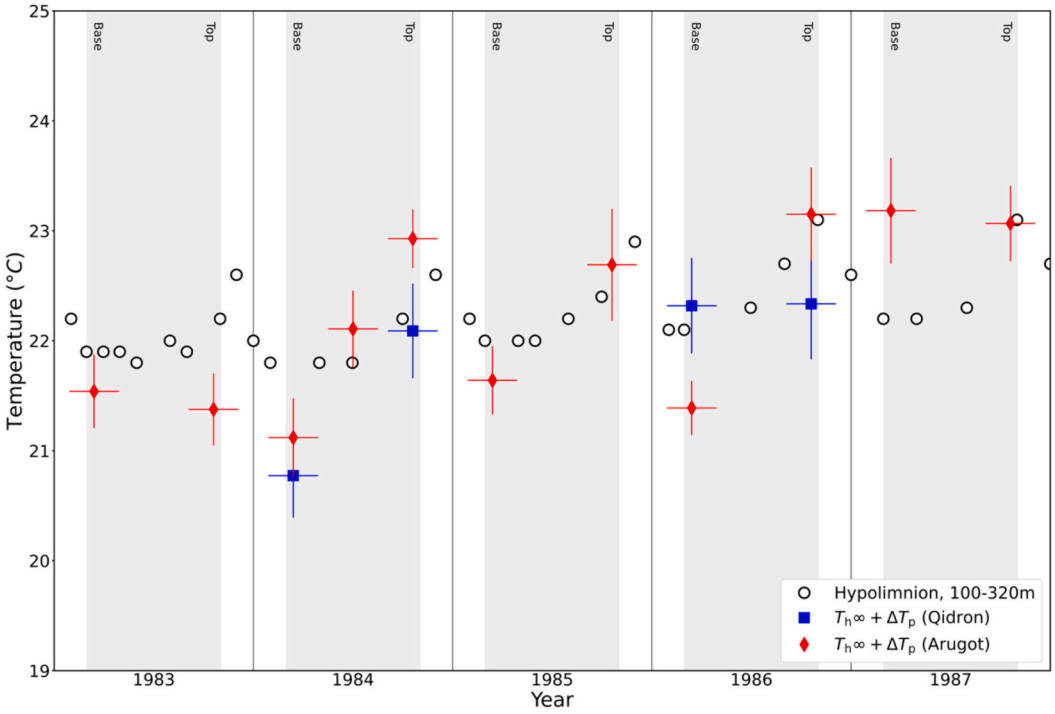

Fig. 8. Reconstructed fluid inclusion temperature record from the Dead Sea, from 1983 to 1987, from two sites: Arugot (red diamonds) and Qidron (blue squares). White circles show monitored Dead Sea bottom water temperature from 1983 to 1987, at water depths of 100–320 m (Anati and Stiller, 1991). (For interpretation of the references to colour in this figure legend, the reader is referred to the web version of this article.)

these ancient halites can be compared to that observed within the synthetic and modern Dead Sea samples.

In case study 1, we demonstrate that the estimated T_f ($T_f \equiv T_{h_{avg}}^{\infty}$) from the synthetic lab-grown halite of 25.3 ± 0.2 °C (2SEM) matches the independently-measured brine temperature of 25.05 ± 0.3 °C; the scatter of T_h^{∞} (23.1–27.4 °C, Δ = 4.3 °C), however, is one order of magnitude larger than both the SEM and the variability of the measured brine temperature. This suggests that the scatter of T_h^{∞} may reflect more than the temperature fluctuations during the experiment, involving processes that modify the volume and/or density of the fluid inclusions. It must be noted, however, that this study used a single temperature sensor submerged in the brine, which could not detect small spatial-scale temperature fluctuations in the flask, such as the heat of crystallization. Future experiments monitoring halite crystallization will employ thermocouples at several positions in the brine to capture small-scale temperature fluctuations at high spatial resolution. On the other hand, if the brine temperature within the water bath is indeed as stable as measured, then the scatter of T_h^{∞} could in fact reflect unresolved non-thermal effects on volume/density. The observed scatter is both above and below the measured brine temperature range, so an explanation is needed that can shift T_h positively and negatively.

In case study 2, the reconstructed T_f record from the modern Dead Sea halite, generally agrees with the instrumental BWT record for the same time period, but does deviate from the BWT record in three cases: low spring (varve base) temperatures in 1984 and 1986; high spring (varve base) temperature in 1987; and a low autumn (varve top) temperature observed in 1983 (Fig. 8). These differences could be due to the difference in water depth between where the halite crystallized (~35 m in the 1980s) versus where the instrumental BWT measurements were taken (100–320 m). Lateral and temporal fluctuations in thermocline depth due to internal waves have been observed, and these fluctuations could potentially account for temperature variations of several degrees at depths of 35 m (Arnon et al., 2019). Nevertheless, the low variance of T_h^{∞} for each Dead Sea halite sample (σ = 0.6–1.7 °C) indicates broad stability of water temperature during halite precipitation. The scatter observed in these samples (weighted mean Δ = 5.5 °C, excluding outliers) is generally larger than that observed within the synthetic halites (Δ = 2.4 °C).

In case study 3, there is no independent temperature proxy with which we can compare reconstructed T_f from Pleistocene-Holocene Death Valley halite. We can, however, compare the precision and scatter of T_h^{∞} with that found in the lab-grown and modern Dead Sea halite. The T_h^{∞} variance observed for samples DV 10–3 and Holocene DV 15–1 is low, with standard deviations of 1.4 °C and 0.8 °C, respectively. The temperature scatter, 6.8 °C and 3.5 °C respectively, is higher than that observed within lab-grown halite but comparable to the scatter observed in the Dead Sea halite.

4.3. *Interpretation of temperatures in the context of depositional environment*

The halites analyzed in this study formed at more or less constant temperatures. The lab-grown samples precipitated in a controlled water bath, the Dead Sea halites are interpreted to have formed at the brine-sediment interface below the thermocline at stable brine temperatures (daily-weekly variability within 0.4 °C) (Arnon et al., 2016), and the Death Valley halites are interpreted to have formed at the bottom of a lake, at most ~90 m deep (Lowenstein et al., 1998). The T_h^{∞} distributions for these samples are Gaussian-like, unimodal, and free of skew, with generally low variance (standard deviations from 0.5 to 1.8 °C), consistent with formation at stable brine temperatures. We interpret the samples as single populations of inclusions trapped at relatively constant temperatures, with the T_f and respective 2SEM uncertainties for each sample reflecting the average brine temperature at the time of halite precipitation.

NA microthermometry may also be used to study halite grown under more variable temperatures. Large temperature variance, signs of multimodality, and even skewed distributions may relate to limnology and seasonality of the depositional environment, and the temperature distributions recorded within halite samples may potentially preserve

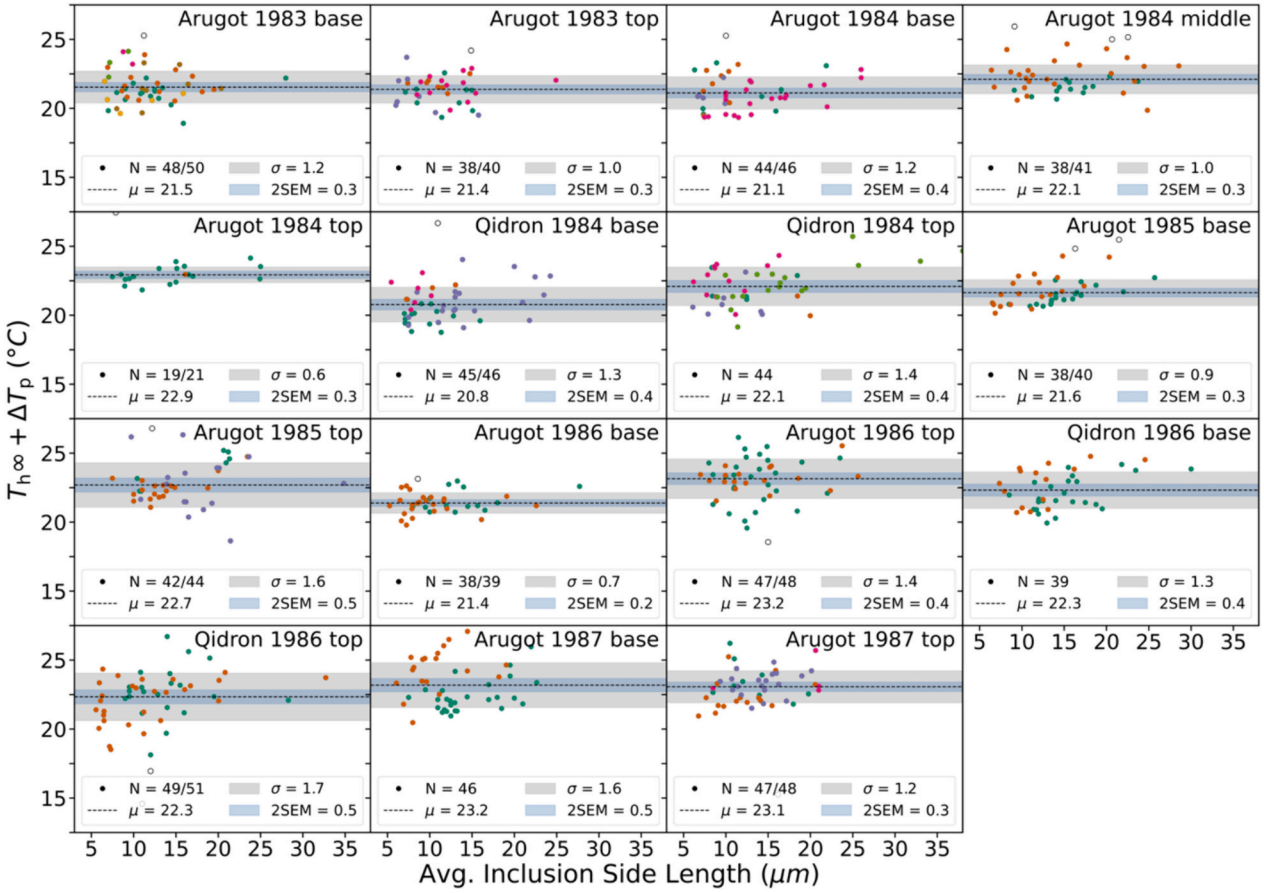

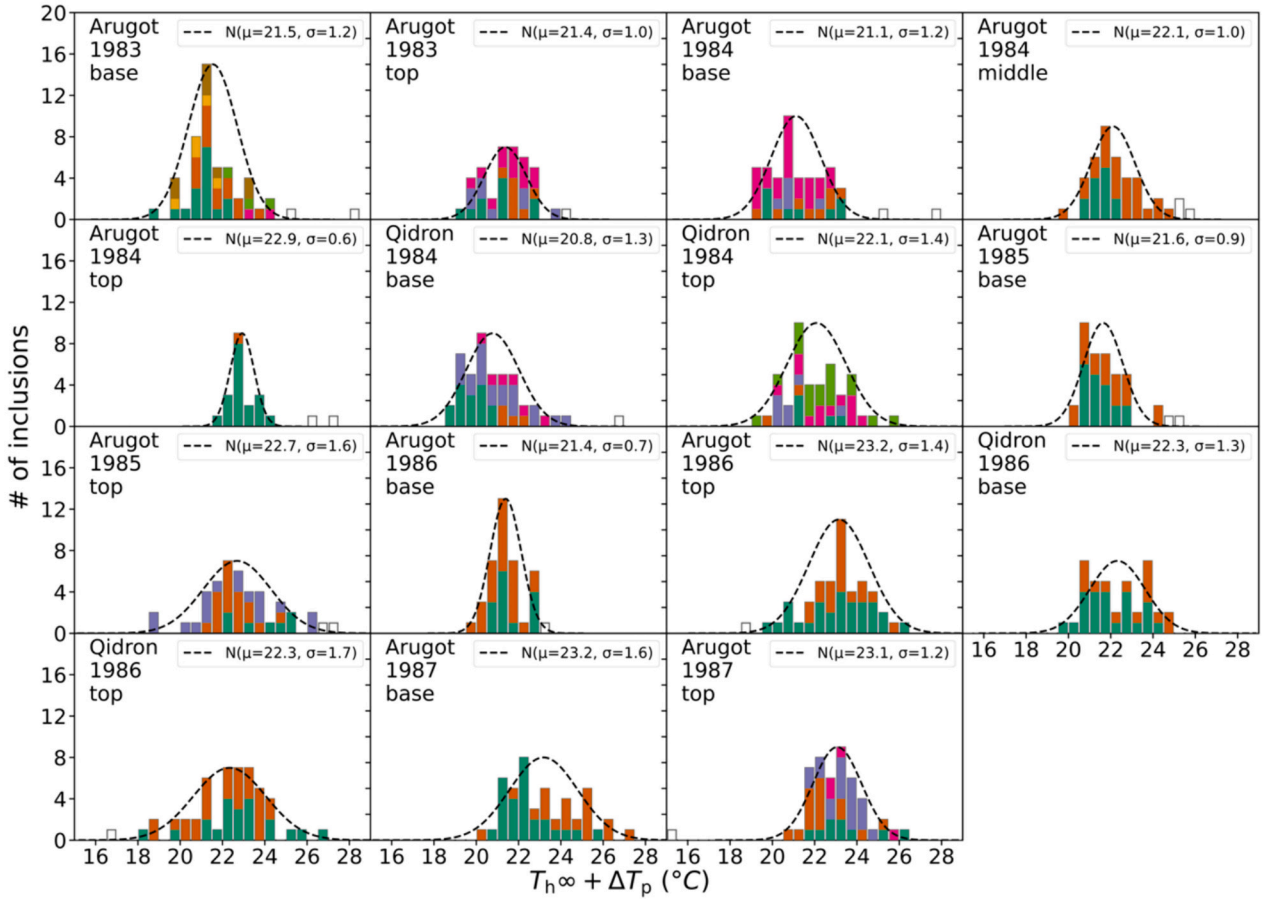

(caption on next page)

Fig. 9. (top) Laplace- and hydrostatic pressure-corrected T_h^∞ vs. fluid inclusion size plots for each Dead Sea varved halite sample, labeled by sample site and interpreted formation year. Colors show individual crystal subsamples. Inclusions larger than ~20 μm average side lengths are at greater risk for deformation, based on minimum/maximum exposure temperatures according to the equations of Guillerm et al. (2020). The hydrostatic pressure-corrected T_h^∞-size plots shown here do not indicate any significant deformation trends. (bottom) Histograms of Laplace- and hydrostatic pressure-corrected T_h^∞ distributions. Colors show individual crystal subsamples. Open scatter plot points/histogram bars indicate outliers that were excluded from statistical analysis based on a 4MAD criterion.

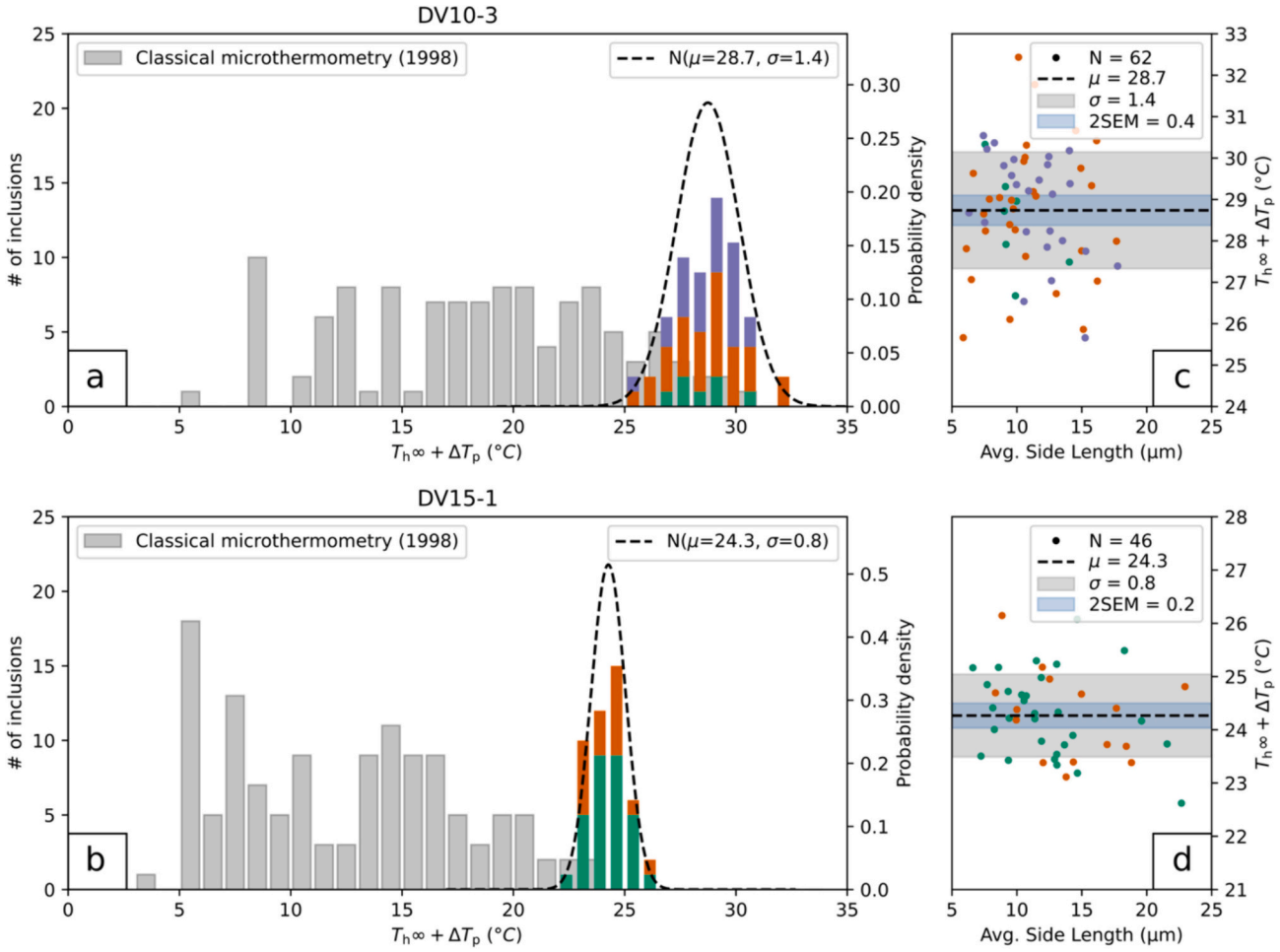

Fig. 10. (a-b) Histogram plots illustrating T_h distributions for two samples from Death Valley core DV93–1, (a) 10–3 (8.7 m; 10.0 ± 3.9 ka) and (b) 15–1 (15.8 m, 26.3 ± 4.8 ka) obtained with NA microthermometry (this study) and with classical microthermometry shown in light gray (Lowenstein et al., 1998). Note, temperatures from this study represent $T_h^\infty + \Delta T_p$ and are colour-labeled for individual subsamples, whereas the data from Lowenstein et al. (1998) are observed homogenization temperatures ($T_{h,obs}$). Dashed black curves are Gaussian fits to the temperatures distributions obtained with NA microthermometry.
(c-d) Plots of Laplace and hydrostatic pressure-corrected homogenization temperatures ($T_h^\infty + \Delta T_p$) vs. average inclusion side length of each inclusion for samples 10–3 (c) and 15–1 (d). Light blue error bars represent two standard errors of the mean (2SEM). Gray error bars represent one standard deviation (σ) from the mean (μ). (For interpretation of the references to colour in this figure legend, the reader is referred to the web version of this article.)

information about the depositional setting itself. For example, halite grown at the air-water interface, within the water column, or even at the bottom of a shallow water body may have experienced rapid changes in temperatures, whereas halite crystallized at the bottom of a deep water body is likely shielded from such short-term temperature variability. The high precision and accuracy of NA microthermometry opens the door to analysis of T_h variability at diurnal and seasonal scales, and with shifting brine depths. Future studies utilizing this method must therefore be preceded by careful sedimentological and petrographic analysis to appropriately interpret T_h distributions and fully understand how and which environmental factors control temperature distributions.

Another important consideration when interpreting temperatures measured from fluid inclusions in halite is the resolution of age/time within the record being analyzed. In the case of varved deposits such as the 1980s Dead Sea halite, crystals are interpreted to form seasonally/sub-annually; the certainty regarding the timing of halite formation allows for seasonal resolution of temperatures. In other halites, such as those from Death Valley DV93–1, less age control limits the interpretation of temperature trends to longer time scales (*i.e.* 10^3 to 10^4 years). Here, for example, we interpret the temperature and age differences between the two Death Valley samples, 24.3 ± 0.2 °C (26.3 ± 4.8 ka) to 28.7 ± 0.4 °C (10.0 ± 3.9 ka) (Δ = 4.4 ± 0.45 °C, 16.3 ± 8.6 kyr), as consistent with glacial-interglacial-scale climate change (Osman et al., 2021).

5. Conclusions

NA microthermometry greatly improves the analytical power of microthermometry performed on fluid inclusions in halite. This method can be used to determine the water temperatures at which halite crystallized for any deposit in the geologic record that has retained primary textures, fabrics, and fluid inclusions. In this study, we tested the

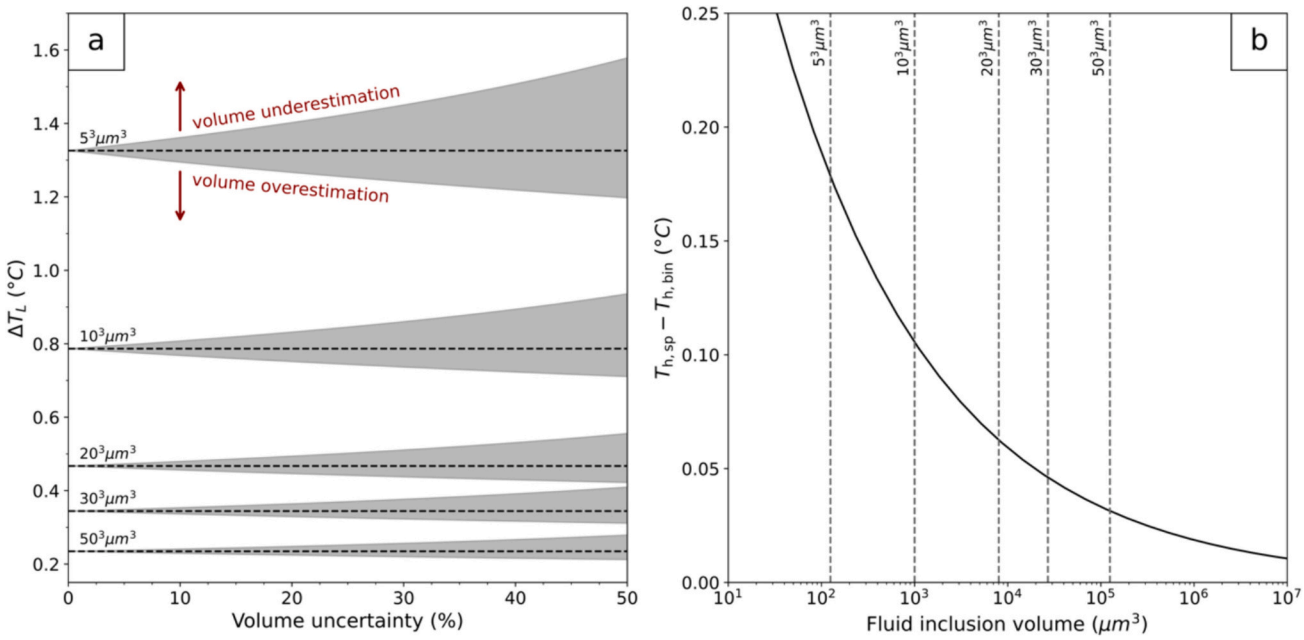

Fig. 11. **(a)** Plot illustrating the effect of FI volume and volume uncertainty on the Laplace correction ΔT_L resulting from surface tension at the liquid-vapor interface. ΔT_L is shown for various nominal FI volumes (5^3 μm^3, 10^3 μm^3, 20^3 μm^3, 30^3 μm^3, 50^3 μm^3) indicated by dashed black lines; gray shaded envelopes illustrate the uncertainty of the Laplace correction due to potential errors in the volume estimates in a range up to ±50% of the nominal volume). Note that volume overestimation results in lower ΔT_L values and volume underestimation results in higher ΔT_L values. The resulting uncertainty on ΔT_L is small ($\lesssim$ 0.05 °C) for large inclusions (>50^3 μm^3) but increases to $\gtrsim$ 0.2 °C for small inclusions (<5^3 μm^3). For inclusions analyzed in this study (5^3 to 30^3μm^3, commonly 10^3 to 20^3μm^3), the overall effect of potential volume over−/underestimations on $T_{h\infty}$ is small and can be considered negligible.
(b): Plot illustrating the effect of FI volume on the temperature range of the metastable two-phase liquid+vapor state (*i.e.* the temperature difference between the onset of metastability, T_{bin}, and the mechanical stability limit, T_{sp}, of the two-phase state). Vertical dashed lines illustrate FI volumes shown in (a). As FI volumes become infinitely large, the difference between T_{bin} and T_{sp} approaches zero; as FI volumes become smaller, however, this difference increases exponentially. In practice we calculated $T_{h\infty}$ for both scenarios $T_{h.obs} = T_{bin}$ and $T_{h.obs} = T_{sp}$ and used the mean value to define the final $T_{h\infty}$. For inclusions measured in this study, the resulting uncertainty is small and can be considered negligible.

accuracy, precision, and reproducibility of T_h measurements made on halite (i) grown in the lab in a controlled temperature water bath and (ii) formed in the modern (1983–1987) Dead Sea. We demonstrate the utility of this method in reconstructing ancient temperatures using (iii) Pleistocene and Holocene halite from the Death Valley DV 93–1 core. The results provide strong evidence that NA microthermometry eliminates the risk of plastic deformation of halite that plagued previous studies that used classical microthermometry on fluid inclusions in halite.

The case studies presented here demonstrate that (i) NA microthermometry-derived temperatures are accurate and precise when compared to lab-grown halite precipitated at known temperatures (25.3 ± 0.2 °C measured T_h^∞ vs. 25.05 ± 0.3 °C observed brine temperature), (ii) reconstructed Dead Sea temperatures from NA-microthermometry are consistent with instrumental temperature records from the same time period: 22.1 ± 1.2 °C overall average fluid inclusion temperature for 1983–1987 versus 22.2 ± 0.4 °C average instrumental BWT temperature for 1983–1987), and (iii) temperature estimates for Pleistocene/Holocene Death Valley halites are significantly more reliable and precise when measured with NA microthermometry compared to standard microthermometry (28.7 ± 0.4 °C for DV10–3; 24.3 ± 0.2 °C for DV15–1).

Aknowledgements

We thank Kennie Leet for use and setup of the HOBO sensor for measuring thermal bath stability. We acknowledge financial support from the National Science Foundation Integrated Earth Systems Program (NSF-EAR 1812741) and the U.S.-Israel Binational Science Foundation grant 2018035. This study is part of the CROSSROADS project and has received funding from the European Union's Horizon 2020 research and innovation programme under the Marie Skłodowska-Curie Action grant agreement No 101029939.

CRediT authorship contribution statement

William D. Arnuk: Writing – original draft, Visualization, Validation, Software, Methodology, Investigation, Formal analysis, Data curation, Conceptualization. **Emmanuel Guillerm:** Writing – original draft, Visualization, Validation, Software, Resources, Investigation, Funding acquisition, Formal analysis, Data curation, Conceptualization. **Tim K. Lowenstein:** Writing – original draft, Validation, Supervision, Resources, Project administration, Investigation, Funding acquisition, Conceptualization. **Yves Krüger:** Writing – review & editing, Validation, Supervision, Resources, Methodology, Investigation, Formal analysis, Conceptualization. **Kristian J. Olson:** Writing – review & editing, Conceptualization. **Nadav G. Lensky:** Writing – review & editing, Resources. **Achim Brauer:** Writing – review & editing, Resources, Funding acquisition.

Declaration of competing interest

The authors declare that they have no known competing financial interests or personal relationships that could have appeared to influence the work reported in this paper.

Data availability

Analytical data and whole-sample summary statistics are available at http://doi.org/10.17632/krncn7bd94.1 (Mendeley Data Repository).

Appendix A. Supplementary data

Supplementary material to this article can be found online at https://doi.org/10.1016/j.chemgeo.2024.122318.

References

Al Ghafri, S., Maitland, G.C., Trusler, J.P.M., 2012. Densities of aqueous $MgCl_2$ (aq), $CaCl_2$ (aq), KI(aq), NaCl(aq), KCl(aq), $AlCl_3$ (aq), and (0.964 NaCl + 0.136 KCl)(aq) at temperatures between (283 and 472) K, pressures up to 68.5 MPa, and molalities up to 6 mol·kg $^{-1}$. J. Chem. Eng. Data 57, 1288–1304.

Al Ghafri, S.Z., Maitland, G.C., Trusler, J.P.M., 2013. Densities of $SrCl_2$ (aq), Na_2SO_4 (aq), $NaHCO_3$ (aq), and two synthetic reservoir brines at temperatures between (298 and 473) K, pressures up to 68.5 MPa, and molalities up to 3 mol·kg $^{-1}$. J. Chem. Eng. Data 58, 402–412.

Anati, D.A., Stiller, M., 1991. The post- 1979 thermohaline structure of the Dead Sea and the role of double-diffusive mixing. Limnol. Oceanogr. 36, 342–353.

Arnon, A., Selker, J.S., Lensky, N.G., 2016. Thermohaline stratification and double diffusion diapycnal fluxes in the hypersaline Dead Sea. Limnol. Oceanogr. 61, 1214–1231.

Arnon, A., Brenner, S., Selker, J.S., Gertman, I., Lensky, N.G., 2019. Seasonal dynamics of internal waves governed by stratification stability and wind: Analysis of high-resolution observations from the Dead Sea. Limnol. Oceanogr. 64, 1864–1882.

Arvengas, A., Davitt, K., Caupin, F., 2011. Fiber optic probe hydrophone for the study of acoustic cavitation in water. Rev. Sci. Instrum. 82, 034904.

Bąbel, M., Schreiber, B.C., 2014. Geochemistry of Evaporites and Evolution of Seawater. In: Treatise on Geochemistry. Elsevier, pp. 483–560.

Benison, K.C., Goldstein, R.H., 1999. Permian paleoclimate data from fluid inclusions in halite. Chem. Geol. 154, 113–132.

Brennan, S.T., Lowenstein, T.K., Cendón, D.I., 2013. The major-ion composition of Cenozoic seawater: the past 36 million years from fluid inclusions in marine halite. Am. J. Sci. 313, 713–775.

Casas, E., Lowenstein, T.K., 1989. Diagenesis of saline pan halite: Comparison of petrographic features of modern, Quaternary and Permian halites. SEPM JSR 59, 724–739.

Caupin, F., 2022. Effects of compressibility and wetting on the liquid–vapor transition in a confined fluid. J. Chem. Phys. 157, 054506.

Caupin, F., 2023. Fluid inclusions in minerals: from geosciences to the physics of water and back. C. R. Phys. 23, 71–87.

Caupin, F., Herbert, E., 2006. Cavitation in water: a review. C. R. Phys. 7, 1000–1017.

Church, C.C., 2002. Spontaneous homogeneous nucleation, inertial cavitation and the safety of diagnostic ultrasound. Ultrasound Med. Biol. 28, 1349–1364.

Davitt, K., Arvengas, A., Caupin, F., 2010. Water at the cavitation limit: Density of the metastable liquid and size of the critical bubble. Europhys. Lett. 90, 16002.

Driesner, T., 2007. The system H_2O–NaCl. Part II: Correlations for molar volume, enthalpy, and isobaric heat capacity from 0 to 1000°C, 1 to 5000bar, and 0 to 1 XNaCl. Geochim. Cosmochim. Acta 71, 4902–4919.

Dutcher, C.S., Wexler, A.S., Clegg, S.L., 2010. Surface tensions of inorganic multicomponent aqueous electrolyte solutions and melts. J. Phys. Chem. A 114, 12216–12230.

El Mekki-Azouzi, M., Tripathi, C.S.P., Pallares, G., Gardien, V., Caupin, F., 2015. Brillouin spectroscopy of fluid inclusions proposed as a paleothermometer for subsurface rocks. Sci. Rep. 5, 13168.

Fall, A., Rimstidt, J.D., Bodnar, R.J., 2009. The effect of fluid inclusion size on determination of homogenization temperature and density of liquid-rich aqueous inclusions. Am. Mineral. 94, 1569–1579.

Gertman, I., Hecht, A., 2002. The Dead Sea hydrography from 1992 to 2000. J. Mar. Syst. 35, 169–181.

Gilg, H.A., Krüger, Y., Taubald, H., Van Den Kerkhof, A.M., Frenz, M., Morteani, G., 2014. Mineralisation of amethyst-bearing geodes in Ametista do Sul (Brazil) from low-temperature sedimentary brines: evidence from monophase liquid inclusions and stable isotopes. Mineral. Deposita 49, 861–877.

Goldstein, R.H., 2001. Fluid inclusions in sedimentary and diagenetic systems. Lithos 55, 159–193.

Goldstein, R.H., Reynolds, T.J., 1994. Systematics of Fluid Inclusions in Diagenetic Minerals. SEPM (Society for Sedimentary Geology).

Guillerm, E., Gardien, V., Ariztegui, D., Caupin, F., 2020. Restoring halite fluid inclusions as an accurate palaeothermometer: Brillouin thermometry versus microthermometry. Geostand. Geoanal. Res. 44, 243–264.

Guillerm, E., Gardien, V., Waldmann, N.D., Brall, N.S., Ariztegui, D., Schwab, M.J., Neugebauer, I., Lach, A., Caupin, F., 2023. Reconstruction of Dead Sea lake level and mass balance back to 237 ka BP using halite fluid inclusions. QSR 303, 107964.

Hampel, F.R., 1974. The influence curve and its role in robust estimation. J. Am. Stat. Assoc. 69, 383–393.

Herbert, E., Balibar, S., Caupin, F., 2006. Cavitation pressure in water. Phys. Rev. E 74, 041603.

Jagniecki, E.A., Lowenstein, T.K., Jenkins, D.M., Demicco, R.V., 2015. Eocene atmospheric CO_2 from the nahcolite proxy. Geology 43, 1075–1078.

Kiro, Y., Goldstein, S.L., Garcia-Veigas, J., Levy, E., Kushnir, Y., Stein, M., Lazar, B., 2017. Relationships between lake-level changes and water and salt budgets in the Dead Sea during extreme aridities in the Eastern Mediterranean. EPSL 464, 211–226.

Koltai, G., Kluge, T., Krüger, Y., Spötl, C., Rinyu, L., Audra, P., Honiat, C., Leél-Őssy, S., Dublyansky, Y., 2024. Geothermometry of calcite spar at 10–50 °C. Sci. Rep. 14, 1553.

Krüger, Y., Stoller, P., Rička, J., Frenz, M., 2007. Femtosecond lasers in fluid-inclusion analysis: overcoming metastable phase states. EJM 19, 693–706.

Krüger, Y., Marti, D., Staub, R.H., Fleitmann, D., Frenz, M., 2011. Liquid–vapour homogenisation of fluid inclusions in stalagmites: Evaluation of a new thermometer for palaeoclimate research. Chem. Geol. 289, 39–47.

Krüger, Y., García-Ruiz, J.M., Canals, À., Marti, D., Frenz, M., Van Driessche, A.E.S., 2013. Determining gypsum growth temperatures using monophase fluid inclusions—Application to the giant gypsum crystals of Naica, Mexico. Geology 41, 119–122.

Krumgalz, B.S., Hecht, A., Starinsky, A., Katz, A., 2000. Thermodynamic constraints on Dead Sea evaporation: can the Dead Sea dry up? Chem. Geol. 165, 1–11.

Lensky, N.G., Dvorkin, Y., Lyakhovsky, V., Gertman, I., Gavrieli, I., 2005. Water, salt, and energy balances of the Dead Sea. Water Resourc. Res. 41 (12).

Lensky, N., Gertman, I., Arnon, A., Ozer, T., Biton, E., Katsenelson, B., Bodzin, R., 2013. Currents and Hydrography of the Dead Sea: A Study for the Salt Recovery Project, 1st Report – July 2012 Survey. Geological Survey of Israel, Israel Oceanographic and Limnological Research.

Li, J., 1996. 100 Kyr Paleoclimate Record from Salt Cores, Death Valley, California. PhD thesis,. State University of New York at Binghamton.

Li, J., Lowenstein, T.K., Brown, C.B., Ku, T.-L., Luo, S., 1996. A 100 ka record of water tables and paleoclimates from salt cores, Death Valley, California. Palaeogeogr. Palaeoclimatol. Palaeoecol. 123, 179–203.

Løland, M.H., Krüger, Y., Fernandez, A., Buckingham, F., Carolin, S.A., Sodemann, H., Adkins, J.F., Cobb, K.M., Meckler, A.N., 2022. Evolution of tropical land temperature across the last glacial termination. Nat. Commun. 13, 5158.

Lowenstein, T.K., Demicco, R.V., 2006. Elevated Eocene atmospheric CO_2 and its subsequent decline. Science 313, 1928.

Lowenstein, T.K., Hardie, L.A., 1985. Criteria for the recognition of salt-pan evaporites. Sedimentology 32, 627–644.

Lowenstein, T.K., Li, J., Brown, C.B., 1998. Paleotemperatures from fluid inclusions in halite: method verification and a 100,000 year paleotemperature record, Death Valley, CA. Chem. Geol. 150, 223–245.

Lowenstein, T.K., Timofeeff, M.N., Brennan, S.T., Hardie, L.A., Demicco, R.V., 2001. Oscillations in Phanerozoic seawater chemistry: Evidence from fluid inclusions. Science 294, 1086–1088.

Lowenstein, T.K., Dolginko, L.A.C., García-Veigas, J., 2016. Influence of magmatic-hydrothermal activity on brine evolution in closed basins: Searles Lake, California. Geol. Soc. Am. Bull. 128, 1555–1568.

Lowenstein, T.K., Olson, K.J., Stewart, B.W., McGee, D., Stroup, J.S., Hudson, A.M., Wendt, K.A., Peaple, M.D., Feakins, S.J., Bhattacharya, T., Lund, S., 2024. Unified 200 kyr paleohydrologic history of the Southern Great Basin: Death Valley, Searles Valley, Owens Valley and the Devils Hole cave. Quat. Sci. Rev. 336, 108751.

Marti, D., Krüger, Y., Fleitmann, D., Frenz, M., Rička, J., 2012. The effect of surface tension on liquid–gas equilibria in isochoric systems and its application to fluid inclusions. Fluid Phase Equilib. 314, 13–21.

McCulloch, D.S., 1959. Vacuole disappearance temperatures of laboratory-grown hopper halite crystals. J. Geophys. Res. 64, 849–854.

Meckler, A.N., Affolter, S., Dublyansky, Y.V., Krüger, Y., Vogel, N., Bernasconi, S.M., Frenz, M., Kipfer, R., Leuenberger, M., Spötl, C., Carolin, S., Cobb, K.M., Moerman, J., Adkins, J.F., Fleitmann, D., 2015. Glacial–interglacial temperature change in the tropical West Pacific: A comparison of stalagmite-based paleo-thermometers. Quat. Sci. Rev. 127, 90–116.

Meng, F., Ni, P., Ge, C., Wang, T., Wang, G., Liu, J., Zhao, C., 2011. Homogenization temperature of fluid inclusions in laboratory grown halite and its implication for paleotemperature reconstruction. Acta Petrol. Sin. 27, 1543–1547.

Morrison, G., 1981. Effect of water on the critical points of carbon dioxide and ethane. J. Phys. Chem. 85, 759–761.

Olson, K.J., Demicco, R.V., Lowenstein, T.K., 2023. Seasonal dynamics of evaporite mineral precipitation, dissolution, and back-reactions in shallow and deep hypersaline lakes. Geochim. Cosmochim. Acta 351, 51–65.

Olson, K.J., Lowenstein, T.K., 2021. Searles Lake evaporite sequences: indicators of late Pleistocene/Holocene lake temperatures, brine evolution, and pCO_2. GSA Bull 113 (11–12), 2319–2334.

Osman, M.B., Tierney, J.E., Zhu, J., Tardif, R., Hakim, G.J., King, J., Poulsen, C.J., 2021. Globally resolved surface temperatures since the Last Glacial Maximum. Nature 599, 239–244.

Rigaudier, T., Lécuyer, C., Gardien, V., Suc, J.-P., Martineau, F., 2011. The record of temperature, wind velocity and air humidity in the δD and δ18O of water inclusions in synthetic and Messinian halites. Geochim. Cosmochim. Acta 75, 4637–4652.

Rigaudier, T., Gardien, V., Martineau, F., Reverdy, G., Lécuyer, C., 2012. Hydrogen and oxygen isotope reference materials for the analysis of water inclusions in halite. Geostand. Geoanal. Res. 36, 51–59.

Roberts, S.M., Spencer, R.J., 1995. Paleotemperatures preserved in fluid inclusions in halite. Geochim. Cosmochim. Acta 59, 3929–3942.

Roedder, E., 1984. Fluid Inclusions: An Introduction to Studies of All Types of Fluid Inclusions, Gas, Liquid, or Melt, Trapped in Materials from Earth and Space, and Their Application to the Understanding of Geologic Processes. Mineralogical Soc. of America, Blacksburg, Va.

Schreiber, B.C., Tabakh, M.E., 2000. Deposition and early alteration of evaporites. Sedimentology 47, 215–238.

Sirota, I., Enzel, Y., Lensky, N.G., 2017. Temperature seasonality control on modern halite layers in the Dead Sea: In situ observations. Geol. Soc. Am. Bull. B31661, 1.

Sirota, I., Enzel, Y., Lensky, N.G., 2018. Halite focusing and amplification of salt layer thickness: From the Dead Sea to deep hypersaline basins. Geology 46, 851–854.

Sirota, I., Enzel, Y., Mor, Z., Ben, Moshe L., Eyal, H., Lowenstein, T.K., Lensky, N.G., 2021. Sedimentology and stratigraphy of a modern halite sequence formed under Dead Sea level fall. Sedimentology 68, 1069–1090.

Spear, N., Holland, H.D., Garcia-Veígas, J., Lowenstein, T.K., Giegengack, R., Peters, H., 2014. Analyses of fluid inclusions in Neoproterozoic marine halite provide oldest measurement of seawater chemistry. Geology 42, 103–106.

Speranza, G., Cosentino, D., Tecce, F., Faccenna, C., 2013. Paleoclimate reconstruction during the Messinian evaporative drawdown of the Mediterranean Basin: Insights from microthermometry on halite fluid inclusions. Geochem. Geophys. Geosyst. 14, 5054–5077.

Steinhorn, I., 1983. In situ salt precipitation at the Dead Sea. Limnol. Oceanogr. 28, 580–583.

Warren, J.K., 2010. Evaporites through time: Tectonic, climatic and eustatic controls in marine and nonmarine deposits. Earth Sci. Rev. 98, 217–268.

Weldeghebriel, M.F., Lowenstein, T.K., 2023. Seafloor hydrothermal systems control long-term changes in seawater [Li^{+}]: Evidence from fluid inclusions. Sci. Adv. 9, eadf1605.

Weldeghebriel, M.F., Lowenstein, T.K., García-Veigas, J., Cendón, D.I., 2022. [Ca^{2+}] and [SO_4^{2-}] in Phanerozoic and terminal Proterozoic seawater from fluid inclusions in halite: The significance of Ca-SO_4 crossover points. EPSL 594 (117), 712.

Zhang, H., Liu, C., Zhao, Y., Mischke, S., Fang, X., Ding, T., 2015. Quantitative temperature records of mid Cretaceous hothouse: Evidence from halite fluid inclusions. Palaeogeogr. Palaeoclimatol. Palaeoecol. 437, 33–41.

Zhang, H., Lü, F., Mischke, S., Fan, M., Zhang, F., Liu, C., 2017. Halite fluid inclusions and the late Aptian sea surface temperatures of the Congo Basin, northern South Atlantic Ocean. Cretac. Res. 71, 85–95.

Zimmermann, H., 2001. On the origin of fluids included in Phanerozoic marine halite—basic interpretation strategies. Geochim. Cosmochim. Acta 65, 35–45.